






Fermi energy, electrical conductivity, and the energy gap of NaNbO_3

Nicole Bein ¹, Brigita Kmet ², Tadej Rojac ², Andreja Benčan Golob ², Barbara Malič ², Julian Moxter ³, Thorsten Schneider ⁴, Lovro Fulanovic ⁴, Maryam Azadeh ⁴, Till Frömmling ⁴, Sonja Egert ⁵, Hongguang Wang,⁶ Peter van Aken ⁶, Jutta Schwarzkopf,⁷ and Andreas Klein ^{1,*}

¹Technische Universität Darmstadt, Institute of Materials Science, Otto-Berndt-Str. 3, 64287 Darmstadt, Germany

²Jožef Stefan Institute, Electronic Ceramics Department, Jamova cesta 39, 1000 Ljubljana, Slovenia

³Technische Universität Darmstadt, Department of Electrical Engineering and Information Technology, High-voltage engineering, Fraunhoferstr. 4, 64283 Darmstadt, Germany

⁴Technische Universität Darmstadt, Institute of Materials Science, Alarich-Weiss-Str. 2, 64287 Darmstadt, Germany

⁵Technische Universität Darmstadt, Eduard-Zintl-Institut für Anorganische und Physikalische Chemie, Alarich-Weiss-Str. 8, 64287 Darmstadt, Germany

⁶Max Planck Institute for Solid State Research, Heisenbergstr. 1, 70569 Stuttgart, Germany

⁷Leibniz-Institut für Kristallzüchtung, Max-Born-Str. 2, 12489 Berlin, Germany



(Received 22 March 2022; accepted 8 July 2022; published 3 August 2022)

The energy of the valence band maximum of NaNbO_3 is determined from the Schottky barrier heights at the contacts with low work function Sn-doped In_2O_3 and high work function RuO_2 by means of x-ray photoelectron spectroscopy with *in situ* interface preparation. The measurements reveal a valence-band edge energy, which is comparable to that of SrTiO_3 and BaTiO_3 . The energy gap of SrTiO_3 and BaTiO_3 is 3.2 eV and comparable to the values of 3.4 eV to 3.5 eV, which are determined by means of optical and electron energy loss spectroscopy for NaNbO_3 . It is therefore expected that the conduction band minimum of NaNbO_3 is also located at a similar energy as the conduction band minimum of SrTiO_3 and BaTiO_3 . If this is the case, it can be expected that donor doping of NaNbO_3 leads to an electrical conductivity, which is comparable to those of donor-doped SrTiO_3 and BaTiO_3 (up to $\sim 1 \text{ S/cm}^{-1}$). In contrast, Sr- and Ca-doped NaNbO_3 bulk ceramics exhibit a room temperature conductivity up to $10 \times 10^{-10} \text{ S/cm}^{-1}$, only slightly higher than that of NaNbO_3 . High-field conductivity measurements and impedance spectroscopy give no indication that the low conductivity is caused by insulating grain boundaries separating electrically conductive grains. It is therefore suggested that the energy gap of NaNbO_3 is substantially higher than the gap of 3.4 eV to 3.5 eV determined from optical spectroscopy reported in literature and from electron energy loss spectroscopy within this paper, as also suggested from electronic structure calculations of LiNbO_3 [*Phys. Rev. B* **77**, 035106 (2008)].

DOI: [10.1103/PhysRevMaterials.6.084404](https://doi.org/10.1103/PhysRevMaterials.6.084404)

I. INTRODUCTION

NaNbO_3 is a prototype antiferroelectric perovskite and one of the two end members of the important lead-free piezoelectric (K, Na) NbO_3 (KNN) [1–3]. Understanding the electrical conductivity of these materials, which are operated at high electric fields, is of particular relevance. The (relatively) high leakage current is a major obstacle for the application of KNN-based ceramics. It has been reported that Mn-doping can reduce the leakage current of NaNbO_3 [4,5]. This behavior is comparable to that of BaTiO_3 , in which Mn is a typical acceptor dopant used in BaTiO_3 -based multilayer ceramic capacitors [6–9]. In BaTiO_3 oxygen vacancies are donors with energy levels close to the conduction band, which will make the material *n*-type. Hence, acceptor doping is necessary to stabilize a low electrical conductivity [10–13]. Donor doping by partially substituting Ti^{4+} by Nb^{5+} or Ba^{2+} by La^{3+} results in *n*-type conduction of BaTiO_3 , indicating that the energy

levels of the donors are close to or even above the conduction band minimum [14].

The relation between band-edge energies and electrical properties, which is related to the alignment of defect energy levels, is well known for semiconducting materials [15–22], but much less studied for dielectric oxides. BaTiO_3 and SrTiO_3 are two intensively studied prototype perovskite-type oxides with comparable valence and conduction band energies [23,24]. The *n*-type conductivity of BaTiO_3 , which is, hence, comparable to that of SrTiO_3 [25,26], has been related to the energetic position of the band edges, which is determined by the orbital contributions to the energy bands [23,27,28]. In BaTiO_3 , the electronic states near the valence band maximum E_{VB} , and those near the conduction band minimum E_{CB} , are formed mostly by the O $2p$ and Ti $3d$ states shown in Fig. 1. In Pb-containing compounds, the hybridization of the (occupied) Pb $6s$ orbitals with the O $2p$ states results in an upward shift of the valence band maximum by more than 1 eV compared to BaTiO_3 illustrated in Fig. 1 in comparison to PbTiO_3 . The higher valence band maximum of these materials is related to their preference for *p*-type

*andreas.klein@tu-darmstadt.de

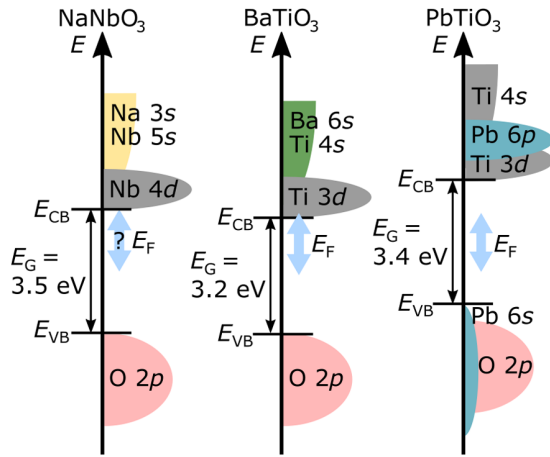


FIG. 1. Band alignment of NaNbO_3 , BaTiO_3 , and PbTiO_3 . All orbitals, which contribute to the conduction and valence band are indicated for each material. In addition, the valence band maximum E_{VB} and conduction band minimum E_{CB} , the band gap values E_{G} and the accessible E_{F} range are illustrated [23,27,28]. For NaNbO_3 the E_{F} range is labeled with a question mark as it is unknown. Donor doping of BaTiO_3 leads to a high electronic conductivity, as E_{F} can be shifted up to the conduction band. A similar upper E_{F} limit can be reached by donor doping of PbTiO_3 , however, it does not lead to electronic conductivity as it is far from the conduction band minimum.

conduction, as the Fermi energy does not need to be as low as in BaTiO_3 on an absolute energy scale to generate positive charge carriers. On the other hand, the higher E_{CB} in PbTiO_3 compared to that of BaTiO_3 prevents n -type conduction upon donor doping or chemical reduction. Similar band structures and conduction behavior to the Pb-based systems apply to Bi-containing perovskite materials.

In NaNbO_3 , neither Na nor Nb is expected to contribute substantially to the valence band states whereas the lowest energy conduction band states are formed mostly from Nb $4d$ orbitals [29]. This situation is similar to that of BaTiO_3 . Also the band gaps of both materials are quite similar with ~ 3.2 eV for BaTiO_3 [30] and 3.4 eV to 3.5 eV in NaNbO_3 [31–38]. It can thus be expected that the E_{VB} , the E_{CB} , and the electrical properties of NaNbO_3 are comparable to those of BaTiO_3 as shown in Fig. 1. This would be consistent with the observation that Mn doping results in a lower conductivity in both perovskites. In general, only a few studies on the electrical conductivity of pure or donor-doped NaNbO_3 are available in literature [39–42].

This paper is aiming at testing this hypothesis by determining the band-edge energies of NaNbO_3 . For this purpose, the interface formation of NaNbO_3 is studied using x-ray photoelectron spectroscopy (XPS) with two different electrode materials: Sn-doped In_2O_3 (ITO) and RuO_2 , which have substantially different work functions of 4.5 eV [43] and 5.6 eV [27,44–46], respectively. Oxide electrode materials are preferable for such studies, as interfacial reactions induced by metal deposition can be avoided [23]. Such reactions can result in Fermi level pinning and thereby impede the determination of band alignment. The use of two different materials can furthermore be used to discuss a potential influence of limitations of band bending by bulk defects [23]. It

is important to exclude such effects for deriving the intrinsic energy band alignment by employing the transitivity rule [46]. For studies of band alignment, we have prepared undoped, Ca-, and Sr-doped NaNbO_3 bulk ceramics using solid state synthesis techniques. The donor-doped NaNbO_3 samples are important in order to verify the hypothesis that donor doping leads to a high electrical conductivity as in donor-doped BaTiO_3 . Ca and Sr are selected as donors to confirm that the effect of doping is not depending on the doping species. For this purpose, the electrical conductivity of the samples is studied using direct current measurements in dependence on electric field and by impedance spectroscopy.

II. EXPERIMENTAL

The polycrystalline NaNbO_3 samples were prepared by solid-state reaction. Na_2CO_3 (99.9%, ChemPur) and orthorhombic Nb_2O_5 (99.9%, Sigma-Aldrich) powder were used as starting materials. For doping CaCO_3 (99.95%, Alfa Aesar) and SrCO_3 (99.994%, Alfa Aesar) was added, respectively. Before mixing, the powders were milled first by attrition milling with isopropanol and yttria-stabilized zirconia balls for 2 h at 500 min^{-1} in case of Nb_2O_5 and by planetary ball milling with acetone and yttria-stabilized zirconia balls for 4 h at 200 min^{-1} for Na_2CO_3 , CaCO_3 , and SrCO_3 . Then the powders were dried at 100°C for 1 h and at 200°C for 2 h, sieved, and dried again at 105°C for 2 h. The dried powders were weighed in a Labmaster 130 glove box (MBraun, Garching, Germany), mixed, and homogenized for 4 h. In case of the doped samples, $\text{Na}_{0.99}\text{Ca}_{0.01}\text{NbO}_3$ and $\text{Na}_{0.99}\text{Sr}_{0.01}\text{NbO}_3$ either CaCO_3 or SrCO_3 was added according to a 1 mol% doping. The homogenization and all following milling steps were done with acetone and yttria-stabilized zirconia balls via planetary ball milling followed by drying at 105°C for 1 h and at 200°C for 2 h, sieving, and drying at 200°C for 2 h. After homogenization, the powders were uniaxially pressed to pellets and calcined for 4 h at 700°C in case of NaNbO_3 in an alumina crucible. For $\text{Na}_{0.99}\text{Sr}_{0.01}\text{NbO}_3$ and $\text{Na}_{0.99}\text{Ca}_{0.01}\text{NbO}_3$ a calcination temperature of 950°C was chosen. A second calcination step was performed at the same conditions after crushing the samples and milling them again for 3 h. After the final milling process for 3 h, pellets with a diameter of 8 mm were pressed isostatically with 200 MPa and sintered in air for 2 h at 1250°C in case of pure and Sr-doped NaNbO_3 and at 1320°C for Ca-doped NaNbO_3 .

For further analysis, the pellets were cut into disks, ground, and polished with diamond paste with a particle size of $0.25 \mu\text{m}$ resulting in a thickness of 0.6 mm to 0.8 mm. Afterwards, a stress-release annealing at 600°C for 1 h with a heating and cooling rate of 5 Kmin^{-1} and 1 Kmin^{-1} was performed, respectively.

Powder x-ray diffraction (XRD) was performed using a X'Pert PRO MPD diffractometer with $\text{Cu } K\alpha_1$ radiation (PANalytical, Almelo, Netherlands) after the two calcination steps as well as after sintering. The microstructure of the samples was obtained by means of scanning electron microscopy (SEM) using a JSM 7600F (Jeol, Tokyo, Japan). The samples' surfaces were polished and thermally etched at 100°C below the sintering temperature beforehand. Nuclear magnetic resonance spectroscopy (NMR) has been performed with a

Triple-Quantum Magic Angle Spinning (3QMAS) pulse sequence. The spectrum was obtained from a Bruker Avance III spectrometer operating at a 7.1 T magnet. A zero-quantum-filtered sequence [47] was employed (see Sec. S1 in the Supplemental Material [48] for more details).

Electrode materials used for probing the interface formation of NaNbO_3 were deposited in the Darmstadt Integrated SYstem for MATerials research (DAISY-MAT), which is an ultrahigh vacuum system consisting of an analysis and several deposition chambers [23]. Prior to electrode deposition, the sample surfaces were cleaned in one of the deposition chambers by heating at 400 °C for 2 h in a low pressure oxygen atmosphere (0.5 Pa). These parameters have been determined by a surface cleaning analysis of ITO [49] and have turned out as good cleaning parameters for several oxide materials used in the research group. With this cleaning procedure, all adsorbed carbonaceous species are removed. For a typical interface experiment, the clean surfaces were first measured in the analysis chamber using x-ray photoelectron spectroscopy (XPS). Then, the electrode material was sputtered stepwise with increasing thickness until the substrate signals were attenuated. After each deposition step, XPS measurements are carried out. ITO was deposited via radio frequency (RF) magnetron sputtering with a power of 25 W under an Ar-flow of 10 sccm and 0.5 Pa at 400 °C, giving a sputter rate of 5 nm min⁻¹ resulting in a polycrystalline film. As it was demonstrated within our working group for the $\text{SrTiO}_3/\text{RuO}_2$ interface, that the deposition temperature of RuO_2 does not change the Fermi level position at the interface [50], direct current (DC) magnetron sputtering performed at room temperature was used to grow the amorphous RuO_2 material on top of the sample. The advantage of a faster deposition process at room temperature since the substrate must not be heated up is, therefore, very convenient as interface experiments are very time consuming. Here, the power was set to 10 W and the pressure to 1 Pa in an Ar/O₂-mixture with 9.25 sccm Ar- and 0.75 sccm O₂-flow resulting in a sputter rate of 3 nm min⁻¹. XPS analysis was performed using a Physical Electronics PHI 5700 spectrometer (Physical Electronics, Chanhassen, MN) with monochromatic Al K α excitation ($h\nu = 1486.6$ eV). All spectra were calibrated according to a sputter-cleaned Ag foil whose Fermi edge was set to 0 eV.

Polarization-field ($P - E$) hysteresis loops and DC-conductivity measurements were carried out at room temperature. For this purpose, the samples were ground to a thickness of about 0.25 mm followed by a stress-release annealing at 400 °C for 1 h. Pt electrodes were sputtered by a Q300TD sputter coater (Quorum, Laughton, East Sussex, UK) on both sides of the disks. Afterwards, the samples were cut in rectangular shapes of about 1.5 mm \times 1.5 mm size. $P - E$ loops were recorded using a TF Analyser 2000 (aixACCT Systems, GmbH, Aachen, Germany) in combination with a high voltage amplifier 20/20C (Trek inc, Lockport, NY). All polarization hysteresis loops were performed at a frequency of 1 kHz. The DC-conductivity measurements started with an electric field of 0.4 kVm⁻¹m, which was increased in 0.2 kVm⁻¹m or 0.4 kVm⁻¹m steps after relaxation of the conductivity. The DC-voltage was applied using an universal high voltage power supply PNChp 30000-2 mup (Heinzinger,

Rosenheim, Germany) while the current was measured by a B2985A electrometer/picoamperemeter (Keysight Technologies, Böblingen, Germany).

Impedance measurements were performed at 325 °C on larger disk-shaped samples with a diameter of about 7 mm to 8 mm and a thickness of 0.34 mm to 0.67 mm. Pt electrodes with 6 mm diameter were sputtered on both sides by the same sputter coater as mentioned earlier. For the measurements, an Alpha-A impedance analyzer (Novocontrol Technologies GmbH & Co. KG, Montabaur, Germany) was used.

Transmission electron microscopy (TEM) specimens were prepared for electron-energy loss measurements by mechanical polishing followed by argon ion milling at liquid nitrogen temperature using a precision ion polishing system (PIPS, model 691, Gatan, Pleasanton, CA) [51]. Low-loss EELS spectra were acquired using the Zeiss SESAM microscope (ZEISS GmbH, Wetzlar, Germany) at an acceleration voltage of 200 kV in TEM mode. The microscope is equipped with an electrostatic Ω -type monochromator (CEOS GmbH, Heidelberg, Germany) and the in-column MANDOLINE energy filter. EELS data were acquired with an energy resolution of 60 meV as determined from the full width at half-maximum of the zero-loss peak (ZLP). For minimizing Cherenkov effects, EELS data were acquired in regions with a thickness of ca. 10 nm to 15 nm as determined via the Fourier-log method [52]. All EELS spectra were calibrated and background-subtracted using a power-law function. We applied a linear fitting method to determine the band gap [53]. Thus, the band-gap energy can be estimated from the intersection of a straight line originating from the background level with a linear fit to the onset of the EELS signal.

III. RESULTS

A. Sample characterization

In order to investigate the occurrence of possible secondary phases and if the samples crystallize in the antiferroelectric phase, XRD, SEM, and electrical measurements (polarization hysteresis loops) were conducted. The XRD measurements [Figs. 2(b) and 2(c)] do not show any secondary phases deviating from the stoichiometric composition of NaNbO_3 . All reflections correspond either to the antiferroelectric P-phase with space group Pbcm (JCPDS 073-0803 [54]) or to the ferroelectric Q-phase with P2₁ma space group (JCPDS 082-0606 [55]). The contributions of the P- and Q-phases can best be identified in the magnified views [56,57]. The small contribution of the ferroelectric Q-phase is further confirmed by nuclear magnetic resonance spectroscopy. The 3QMAS spectrum, see Fig. S1 in the Supplemental Material [48], exhibits two signals corresponding to the two crystallographic sites of NaNbO_3 . It has previously been demonstrated (see, e.g., [58]) that the symmetry of the Na(1) signal is sensitive to the local structural differences between P- and Q-phase NaNbO_3 . In the XRD patterns [Figs. 2(b) and 2(c)], the peaks of the doped samples are slightly shifted to higher 2θ values, which further indicates a decrease of the lattice constant upon doping. The ionic radius of Na⁺ is 1.39 Å [59] for a 12-fold coordination. In comparison, those of Sr²⁺ and Ca²⁺ are

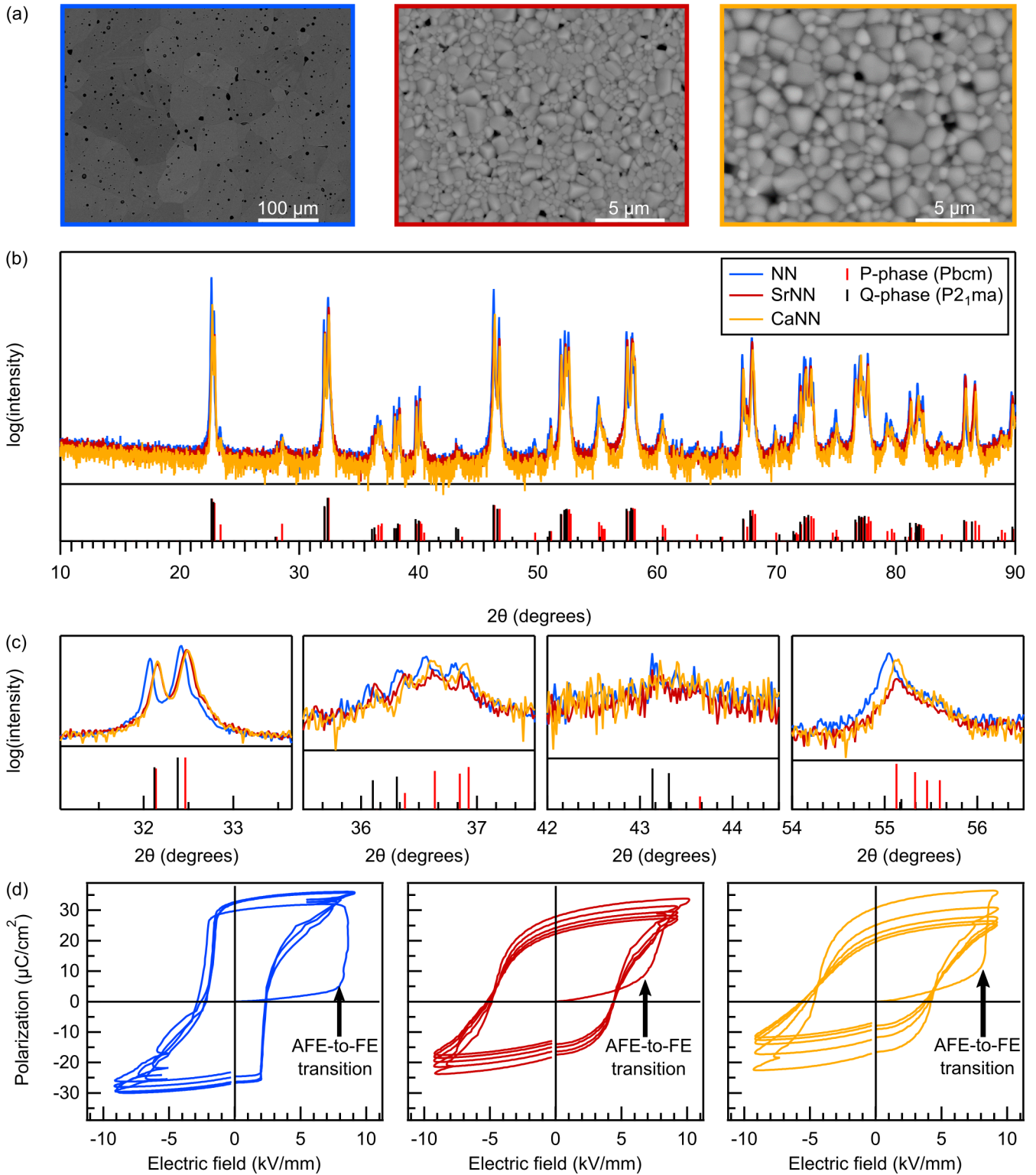


FIG. 2. Comparison of pure NaNbO₃ (blue), Sr-doped NaNbO₃ (red), and Ca-doped NaNbO₃ (yellow). (a) SEM images taken in the secondary electron mode; (b) x-ray diffraction patterns including the reflexes of the antiferroelectric P-phase (red bars) and the ferroelectric Q-phase (black bars); (c) magnified views of the diffraction patterns; and (d) $P - E$ -loops measured at a frequency of 1 kHz.

1.44 Å [59] and 1.34 Å [59], respectively. We attribute the lower lattice constant of the Sr-doped sample to the presence of Ca, which is observed in the XPS survey spectra (see Fig. 3). In the survey spectra, a substantial amount of Ca is visible in the Na_{0.99}Sr_{0.01}NbO₃, which exceeds that of Sr. It

is not clear what the origin of this Ca impurity is, however, it seems only to be present at the surface as energy-dispersive x-ray spectroscopy (EDXS) measurements, shown in Fig. S2 in the Supplemental Material [48], do not detect any Ca traces throughout the bulk material. We note that Ca is a common

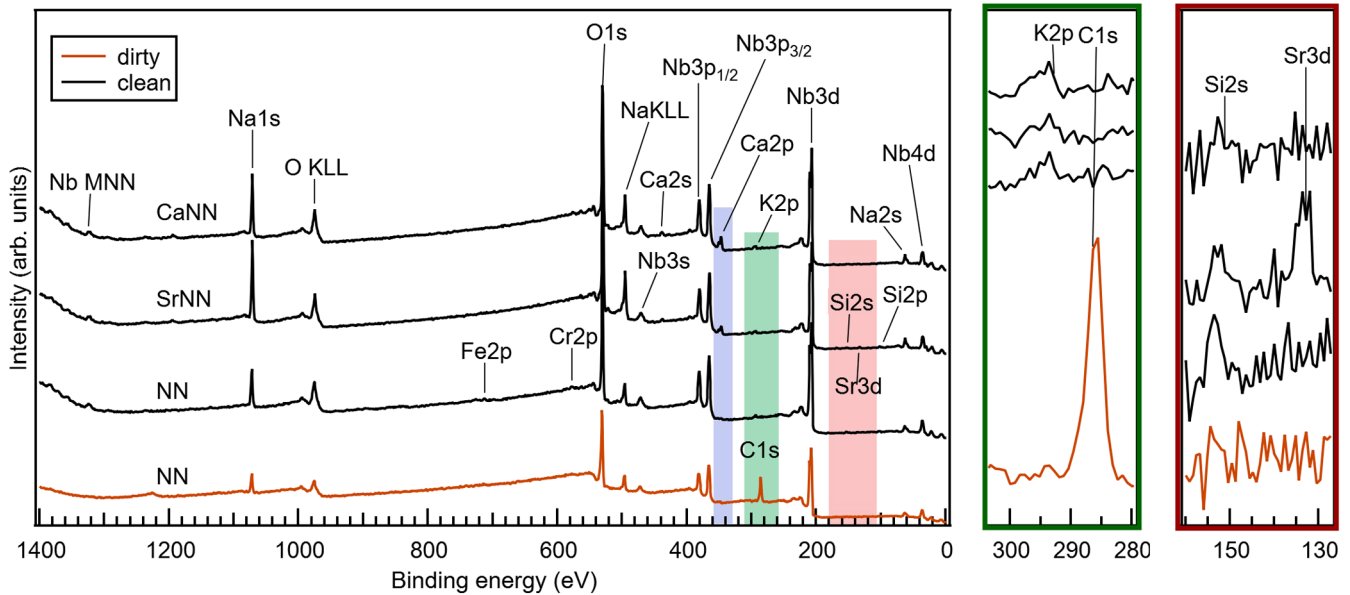


FIG. 3. XPS-survey spectra of an as prepared NaNbO_3 sample (brown) and a cleaned NaNbO_3 as well as Ca- and Sr-doped NaNbO_3 ceramic pellets (black). The two close-ups at the right show magnified views to reveal carbon, potassium, silicon, and strontium species at the surface.

impurity in perovskites and also present in small amounts in the undoped NaNbO_3 . We also observe Ca frequently at clean BaTiO_3 and SrTiO_3 surfaces with XPS (see e.g., [60]).

The microstructure of pure NaNbO_3 (blue), Sr-doped NaNbO_3 (red), and Ca-doped NaNbO_3 (yellow) are shown in Fig. 2(a). No secondary phases deviating from the stoichiometric composition of NaNbO_3 are observed within the detection limits of SEM investigations confirming the XRD results. The average grain size, which is estimated by the line intercept method, is decreasing with doping from about $90\ \mu\text{m}$ to $0.9\ \mu\text{m}$ and $1.5\ \mu\text{m}$ for $\text{Na}_{0.99}\text{Sr}_{0.01}\text{NbO}_3$ and $\text{Na}_{0.99}\text{Ca}_{0.01}\text{NbO}_3$, respectively. Such a reduction of the grain size with doping is commonly seen for other NaNbO_3 -based samples [61,62] and other perovskite materials, e.g., BTO [63,64]. This effect is often explained by a slow grain boundary migration due to the dopants [65–67].

The polarization hysteresis loops illustrated in Fig. 2 verify the results of the XRD measurements that the majority of the sample is in the antiferroelectric state. For all three sample types linear increase of polarization is observed in the first half cycle followed by an abrupt jump in polarization and a subsequent ferroelectric behavior. This is in line with the well-known irreversible electric-field-induced antiferroelectric to ferroelectric phase transition of NaNbO_3 [68,69]. Hysteresis loops measured at lower frequencies showed a leaky behavior for the Ca- and Sr-doped samples and prohibited the application of fields $>3\ \text{kV/mm}$ (see Fig. S4 in the Supplemental Material [48]).

XP survey spectra of the samples are displayed in Fig. 3. The lower two spectra show a NaNbO_3 sample before (brown) and after (black) the surface cleaning by heating in oxygen. Sodium, niobium, oxygen, and carbon can be identified before the cleaning process. The carbon species are no more visible after heating. This increases the intensities of the sample emissions and reveals traces of impurities as potassium and silicon.

Silicon is most likely resulting from grinding the surface with silicon carbide paper. Potassium is the most significant impurity in the Na_2CO_3 starting powder (99.9%, ChemPur) for synthesis, according to the provider. As the small $\text{K}\ 2p$ peak is observed for all samples and the fact that potassium is very volatile [70], we assume that potassium is diffusing to the surface during the sample cleaning procedure. Undoped NaNbO_3 also exhibits small amounts of iron and chromium, which might originate from the holding mask of the sample holder.

Despite their nominally low concentration, the dopants Ca and Sr are observed in the wide scan survey spectra of the clean samples. A quantification of the intensities reveals that the amount of Ca is 10 mol% to 20 mol%, which is higher than the concentration of Sr in $\text{Na}_{0.99}\text{Sr}_{0.01}\text{NbO}_3$ and much higher than the intended doping concentration. This is also evident from comparing the intensity of the most intense Ca and Sr peaks visible in the blue and red region in Fig. 3, respectively. The observation of such high concentrations of Ca indicates segregation to the surface. No enhanced Ca concentration in the bulk and no Ca segregation to the grain boundaries is observed by means of EDXS. Figures S2 and S3 in the Supplemental Material [48] show the bright field scanning transmission electron microscopy (STEM) image of a grain boundary (GB) with the corresponding EDXS spectrum and the intensity maps of Na K, Nb K, Ca K, and Sr K lines for $\text{Na}_{0.99}\text{Sr}_{0.01}\text{NbO}_3$ and $\text{Na}_{0.99}\text{Ca}_{0.01}\text{NbO}_3$, respectively.

Figure 4 shows EELS measurements in a transmission electron microscope of a pure (blue) and Sr-doped (red) NaNbO_3 sample. From the onset of the EELS signal the band gap E_G can be determined. The evaluated value for NaNbO_3 and $\text{Na}_{0.99}\text{Sr}_{0.01}\text{NbO}_3$ is $(3.53 \pm 0.06)\ \text{eV}$ and $(3.54 \pm 0.06)\ \text{eV}$, respectively. Slightly smaller band-gap energies are obtained by XPS. The energetic distance between

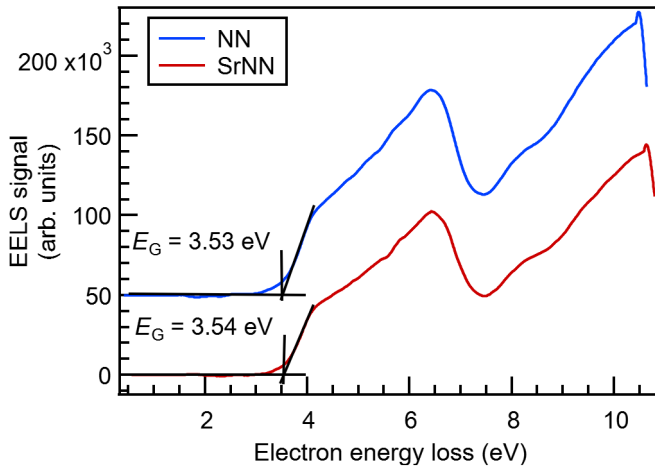


FIG. 4. Determination of the band gap E_G for a pure (blue) and Sr-doped (red) NaNbO_3 bulk ceramic sample by means of the onset of the EELS signal.

the O $1s$ peak and the onset of the energy loss spectrum can be used as a measure of the energy gap of the material [71,72]. In Fig. S5 in the Supplemental Material [48], the corresponding O $1s$ lines of pure, Sr- and Ca-doped NaNbO_3 , and two nominally undoped NaNbO_3 thin films grown by pulsed laser deposition are illustrated. The extracted value for bulk ceramic NaNbO_3 is 3.23 eV. Due to some uncertainties in the evaluation, which are discussed in the Supplemental Material [48], the band gap values extracted from EELS are after all more reliable. Band gaps determined by means of optical spectroscopy are in the range of the ones measured by EELS, with values between 3.4 eV to 3.5 eV [31–38] supporting the assumption that the EELS measurements are more reliable. It is noted, however, that calculations using the GW technique (including the Green's function G and the dynamical screened interaction W) for LiNbO_3 indicate that the actual band gap is substantially (~ 1 eV) higher than that measured optically,

which is caused by quasiparticle and electron-hole attraction effects [73,74].

B. Interface analysis

The Na $1s$, O $1s$, In $3d$, and Nb $3d$ core level emissions recorded in the course of ITO deposition onto $\text{Na}_{0.99}\text{Sr}_{0.01}\text{NbO}_3$ are shown in Fig. 5. The valence bands of the clean sample and for a thick ITO film are illustrated as well. In order to follow the evolution of the Fermi energy in the course of interface formation, the binding energy differences of the core levels and the valence band maximum are required. These are indicated above the spectra of the cleaned surface.

The Na $1s$ emission can be decomposed into three components. The most intense component is associated with the bulk NaNbO_3 emission, whereas the two emissions at higher and at lower binding energy are attributed to surface components. Related surface components are also observed in literature for NaNbO_3 [75–77], KNbO_3 [78,79], and discussed extensively for barium in BaTiO_3 [60,80–87] and (Ba, Sr) TiO_3 [88–90]. Different explanations are given in literature for the origin of the surface component. These include surface contamination such as carbonates or hydroxides [75,77,79,86], A-site rich oxide layers including Ruddlesden-Popper phases [60,76,85,87], undercoordinated A-site atoms at the surface [78,80,89], surface relaxation effects [82,88], and surface dipoles [83,84]. As we do not observe substantial amounts of carbon and a symmetric O $1s$ emission, we exclude surface contamination as the origin of the Na $1s$ surface species.

The intensities of the NaNbO_3 -related core level lines are decreasing and the In $3d$ intensity is increasing in the course of ITO deposition. While no changes in the line shape of the Nb $3d$ peak are observed, the intensity ratio of the Na $1s$ surface component to the Na $1s$ bulk component is increasing with ITO thickness. Similar effects have also been observed for the Ba surface components during interface

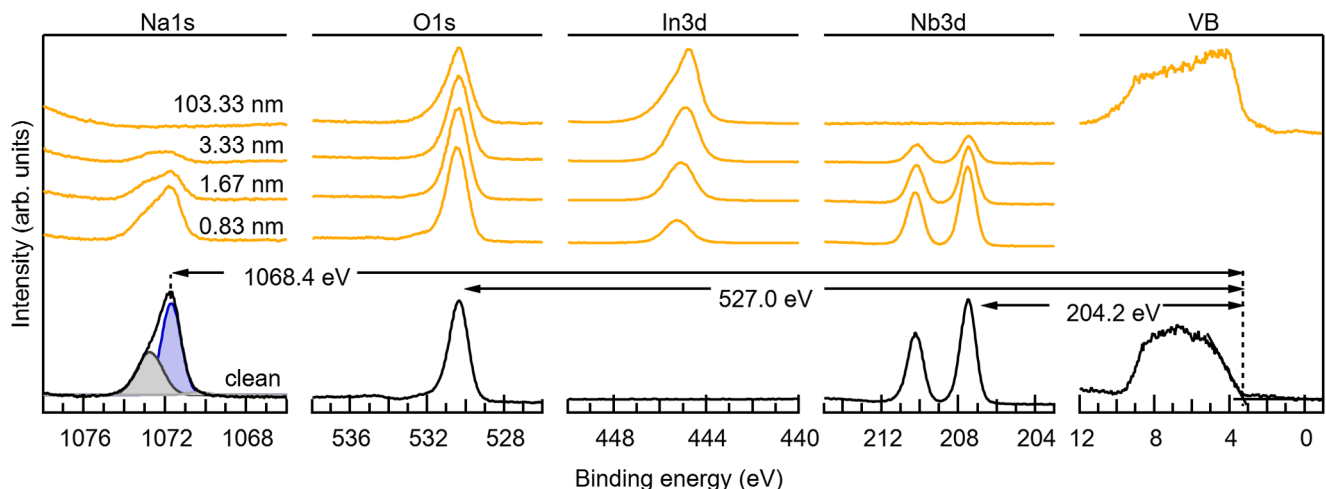


FIG. 5. Na $1s$, O $1s$, In $3d$, and Nb $3d$ core level and valence band spectra of a Sr-doped NaNbO_3 bulk ceramic sample in the course of ITO deposition. The black lines belong to the cleaned sample, whereas the yellow spectra are measured after depositing a few nanometers of ITO on top. The bulk and surface components of the Na $1s$ emission line are colored in blue and grey in the clean XP spectrum. Arrows mark the core-level-to-VBM-distance for each core level of the clean sample.

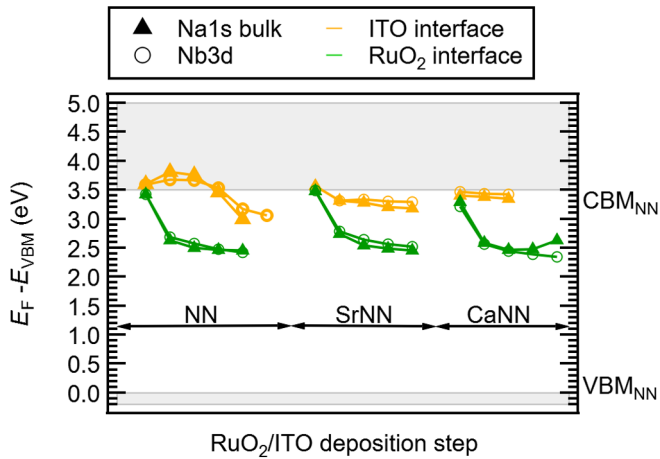


FIG. 6. Evolution of the Fermi energy at the surface of undoped, Sr-doped, and Ca-doped NaNbO_3 in the course of ITO (yellow) and RuO_2 (green) deposition. The Fermi level shift are extracted from the core level lines by subtracting the corresponding core-level-to-VBM-distance indicated in Fig. 5. For ITO the total deposition time per step was 10 s, 20 s, 40 s, 80 s and 160 s with a deposition rate of 5 nm s^{-1} , while for RuO_2 the total deposition time per step was 20 s, 40 s, 80 s, 160 s with a deposition rate of 3 nm s^{-1} . The initial Fermi level positions are affected by charging, due to the low conductivity of the samples.

formation [83,90] and are likely related to changes in the electrostatic boundary conditions rather than to an interface reaction and the formation of a different chemical compound.

The evolution of the Fermi energy in the course of the deposition of ITO (yellow) and RuO_2 (green) onto NaNbO_3 , $\text{Na}_{0.99}\text{Sr}_{0.01}\text{NbO}_3$, and $\text{Na}_{0.99}\text{Ca}_{0.01}\text{NbO}_3$ is shown in Fig. 6. The Fermi level positions derived for the clean sample surfaces are affected by charging of the samples during the XPS measurements due to their low conductivity, particularly for undoped NaNbO_3 . After deposition of a ~ 2 -nm-thick film of ITO or RuO_2 , surface charging disappears due to the high electrical conductivity of the films and their electrical contact with the sample holder [91]. The latter is established by depositing a Pt contact on one edge of the surface before the experiment.

The $\text{Nb } 3d$ and the bulk $\text{Na } 1s$ bulk component exhibit parallel binding energy shifts in the course of ITO or RuO_2 deposition, confirming that the shifts are caused by changes of the Fermi energy. According to Fig. 6, the Fermi energy at the $\text{NaNbO}_3/\text{ITO}$ and $\text{NaNbO}_3/\text{RuO}_2$ interfaces are largely independent of the doping and are given by 3.2 eV to 3.4 eV for ITO and by 2.5 eV to 2.7 eV for RuO_2 . Studies of the variation of the Fermi level conducted in our research group on many different oxide materials, e.g., Fe_2O_3 , $(\text{Ba,Sr})\text{TiO}_3$, $\text{Pb}(\text{Zr,Ti})\text{O}_3$, BiVO_4 , BiFeO_3 , showed that the upper and lower Fermi level limits in any of these oxides is consistently very close to the Fermi level found at the interface of the same oxide to ITO or RuO_2 [27]. Therefore, the Fermi levels determined at the interface to ITO and RuO_2 can be considered as a measure of the upper and lower Fermi level within an oxide material. Assuming a band gap as determined from the electron energy loss signal (see gray area in Fig. 6), the

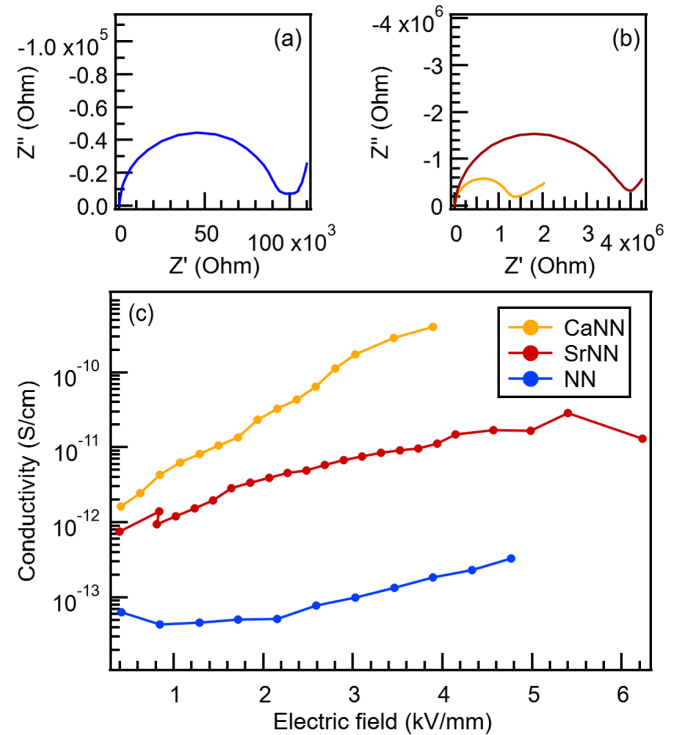


FIG. 7. Impedance measurements of pure NaNbO_3 shown in (a), Sr- (red) and Ca-doped NaNbO_3 (yellow) depicted in (b) and DC-conductivity of NaNbO_3 (blue), Sr- (red) and Ca-doped NaNbO_3 (yellow) as a function of electric field illustrated in (c). The conductivity values are taken after relaxation of the samples for each electric field step.

Fermi energy at the $\text{NaNbO}_3/\text{ITO}$ interfaces will be close to the minimum of the conduction band.

C. Electrical measurements

DC-conductivity measurements were carried out at room temperature as a function of electric field between 0.4 kV mm^{-1} to 6.2 kV mm^{-1} . The measured conductivity curves for NaNbO_3 , $\text{Na}_{0.99}\text{Sr}_{0.01}\text{NbO}_3$, and $\text{Na}_{0.99}\text{Ca}_{0.01}\text{NbO}_3$ are displayed in Fig. 7(c). The conductivity of all samples increases nearly linear with electric field, but remains below $5 \times 10^{-10} \text{ S/cm}^{-1}$.

Nyquist plots for pure NaNbO_3 (blue), Sr- (red) and Ca-doped NaNbO_3 (yellow) are illustrated in Fig. 7(a) and 7(b). The corresponding impedance measurements were done at 325°C . For all three samples one clear semicircle can be identified.

IV. DISCUSSION

For SrTiO_3 and BaTiO_3 , XPS analysis of interfaces with Sn-doped In_2O_3 and of clean donor-doped or reduced surfaces consistently reveal Fermi energies of $> 3 \text{ eV}$ above the valence band maximum [23,46,60,92,93]. Combining this with their band gaps of 3.2 eV [30], the XPS measurements indicate a Fermi energy near the conduction band minimum. This is consistent with the electrical properties. The high electrical conductivity of $\sim 1 \text{ S/cm}$, which can be reached with

reduced and with donor-doped SrTiO₃ and BaTiO₃ [25,26,94–96], are only possible with carrier concentrations of $1 \times 10^{19} \text{ cm}^{-3}$ to $1 \times 10^{20} \text{ cm}^{-3}$ and hence with Fermi energies near the minimum of the conduction band.

The XPS data recorded at the interfaces suggest that the Fermi level in NaNbO₃ can be shifted to values $\sim 3.2 \text{ eV}$. This is similar to the Fermi energies observed at the clean surfaces of Sr-doped and Ca-doped NaNbO₃. The latter values might actually be a bit lower, as charging of the XP spectra cannot be completely excluded. The band gap of NaNbO₃ obtained from the EELS signal is 3.5 eV . In comparison with SrTiO₃ and BaTiO₃, it is therefore expected that the Fermi energy can be shifted close to the conduction band minimum in NaNbO₃. A Fermi energy close to the conduction band minimum would correspond to a high concentration of free (non trapped) charges. Donor-doped NaNbO₃ should thus be highly electronically conducting, similar to donor-doped SrTiO₃ and BaTiO₃. This evidently contradicts the electrical measurements of the donor-doped NaNbO₃ samples with a conductivity ranging from $7.6 \times 10^{-13} \text{ S/cm}^{-1}$ to $1.5 \times 10^{-11} \text{ S/cm}^{-1}$ and from $1.6 \times 10^{-12} \text{ S/cm}^{-1}$ to $4.1 \times 10^{-10} \text{ S/cm}^{-1}$ with an electric field running from 0.4 kV mm^{-1} to 3.9 kV mm^{-1} for Na_{0.99}Sr_{0.01}NbO₃ and Na_{0.99}Ca_{0.01}NbO₃, respectively.

One question related to the present study is to which extent the limits of the Fermi energy, which are related to limits of electrical conductivity, are connected to the energy band alignment of the materials as suggested by the alignment of defect energy levels [17,22,23,97]. A determination of the band alignment of NaNbO₃ with other perovskite oxides is possible by applying the transitivity rule to the Fermi level positions at the interfaces [46]. It is necessary, however, to rule out Fermi level pinning effects, which restrict either the upward or the downward shift of the Fermi energy [23]. The Fermi energies at the NaNbO₃/ITO and the NaNbO₃/RuO₂ interfaces differ by 0.8 eV , which is considerably smaller than the difference observed at interfaces of the same two materials with other oxides [23,27,46,98]. This indicates that some Fermi level pinning is involved at least at one of the two interfaces. At present, we have no clues as to whether the Fermi energy cannot be higher than observed at the NaNbO₃/ITO interface, and/or whether it cannot be lower at the NaNbO₃/RuO₂ interface. In case the NaNbO₃/ITO interface is unpinned, we would extract similar valence band maximum energies of SrTiO₃, BaTiO₃, and NaNbO₃, which corresponds to the comparison discussed in the previous paragraph. In contrast, if the NaNbO₃/RuO₂ interface is unpinned as in the case of BiVO₄ [99], the valence band maximum of NaNbO₃ would be 0.7 eV to 0.8 eV higher than that of BaTiO₃ and SrTiO₃ [50,60]. Expecting similar Fermi level limits, it should be possible to raise the Fermi energy far above the conduction band minimum in NaNbO₃. The two scenarios are compared in Fig. 8.

Donor-doped BaTiO₃ exhibits a narrow range of donor concentrations, for which a low resistivity in the range of $1 \Omega \text{ cm}$ is observed [14,63,94,95,100]. For La-doping, for example, the small resistivity regime with values around $1 \Omega \text{ cm}$ runs from $0.10 \text{ mol}\%$ to $0.25 \text{ mol}\%$. Below a La-concentration of $0.1 \text{ mol}\%$ the dopants are compensated by electrons. An increase in doping concentration leads to a reduction of resistivity. For higher donor concentration, the donors are

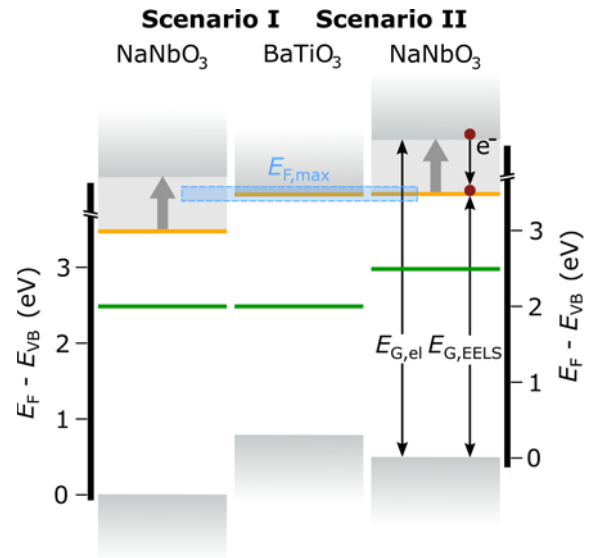


FIG. 8. Energy band diagram of BaTiO₃ and NaNbO₃. The grey rectangles represent the valence and conduction band. Scenario I and II show the band alignment in case the E_F position obtained with RuO₂ (green) and ITO (yellow) is taken for the alignment, respectively. The band gap measured with EELS $E_{G,EELS}$ as well as hypothetical electrical band gap $E_{G,el}$ are indicated in scenario II for NaNbO₃. The difference in the band gap values is illustrated by a grey arrow. The electron of a possible exciton formed in case of the optical and EELS investigations reducing the measured band gap is shown as well.

preferentially compensated by intrinsic defects such as barium (V''_{Ba}) or titanium vacancies (V''_{Ti}). The increase of resistivity can then be assigned to the formation of insulating grain boundaries due to the segregation of acceptor-like cation vacancies to grain boundaries [63,94,100]. In the low resistivity regime, the positive temperature coefficient of resistivity (PTCR) effect can be observed. In donor-doped BaTiO₃, this resistivity jump occurs at the Curie temperature (T_C) and can be explained by the Heywang-Jonker-model [94,101], which is also based on grain boundary potential barriers.

If insulating grain boundaries, caused by segregation of Na vacancies, are the origin of the insulating nature of donor-doped NaNbO₃, a varistor effect as in zinc oxide (ZnO) might be observed. The varistor effect is expressed by a small conductivity at low voltages followed by a nonlinear increase at a certain threshold voltage [102]. The effect originates from the coexistence of conductive grains and insulating grain boundaries [103]. At low voltages, the potential barrier at the grain boundaries hinders the electrons from moving through the sample. At a certain threshold voltage, these barriers can be overcome, resulting in an abrupt conductivity increase. The varistor effect has also been observed for BaTiO₃ and SrTiO₃ based systems [101,104–107] as well as theoretically [108]. The field dependent electrical conductivity shown in Fig. 7(c) does not reveal a typical varistor behavior but a gradual increase of conductivity with applied electric field for donor-doped samples. This increase might be induced by some resistive heating of the sample during the measurement with high voltages applied. Assuming conductive grains, it is possi-

ble to calculate the voltage drop across a single grain boundary from the maximum electric field applied to the samples before breakdown, the sample thickness, and the average grain size. The contribution of the conductive grains to the overall resistance is thereby neglected and it is assumed that the voltage drops only across the grain boundaries. Therefore, the sample thickness can be divided by the number of grain boundaries. A voltage drop of 6 V per grain boundary or higher was reached for all samples. The voltages for which a varistor effect in BaTiO₃ or (Ba,Sr)TiO₃ is observed, range from 0.1 V to 1 V per grain boundary [104,107]. The breakdown voltage in commercial ZnO varistors is 3 V per grain boundary [102,103]. Therefore, we assume that the threshold voltage for a potential varistor effect should have been reached in case of the donor-doped NN samples. The high field conductivity measurements are therefore not consistent with the presence of conducting grains separated by insulating grain boundaries. This is further corroborated by the impedance measurements. Figures 7(a) and 7(b) indicate single semicircles for Na_{0.99}Sr_{0.01}NbO₃, Na_{0.99}Ca_{0.01}NbO₃, and pure NaNbO₃. In case of grain boundary contribution, a second semicircle should emerge at high frequencies. Furthermore, frequency dependent permittivity measurements do not show any relaxation effects resulting from grain boundary contributions below 10×10^4 Hz (see Fig. S6 in the Supplemental Material [48]).

We finally propose that the discrepancy between the observed Fermi level positions and the electrical properties of NaNbO₃ is explained by a band gap, which is considerably higher than the one measured with EELS and the highest reported band gap from optical measurements of 3.5 eV [33,35–37]. This situation is similar to that of LiNbO₃, in which the fundamental energy gap, i.e., the energetic distance between the fully occupied valence band and the completely empty conduction band, is more than 1 eV higher than the one measured by optical techniques. This result has been concluded from GW calculations and is explained by quasiparticle properties [73,74]. During optical measurements an electron is excited from the valence to the conduction band. These two generated charges, however, can interact with each other and form an exciton, which lowers the measured optical band gap. Optical properties do, therefore, not properly reflect the band gap in LiNbO₃ due to this strong electron-hole interaction. Similar effects are present in organic semiconductors. The difference between the electronic transport gap, taking polarization of the molecules due to removal or addition of an electron into account, and the optical gap, the exciton binding energy, is also of the order of 1 eV [109,110]. The large difference between the transport and the optical gap is related to the localized nature of the electronic states. The present study indicates that a similar situation may be encountered in NaNbO₃. This is reasonable, as the electronic structure of NaNbO₃ is comparable to that of LiNbO₃ with highly localized Nb 4*d*-derived states at the conduction band minimum [29,73]. The effect of an exciton formation lowering the measured band gap by XPS, optical and electron energy loss spectroscopy is depicted in Fig. 8. The consequence would be a much larger electrical band gap, which would explain

the low conductivity measured in this study. Independent on which scenario I or II is correct, the maximum Fermi level position $E_{F,\max}$ would be much below the conduction band in NaNbO₃. This situation is different from the one in BaTiO₃, where the E_F can reach the conduction band resulting in a highly conductive sample.

V. SUMMARY AND CONCLUSIONS

The Fermi energy positions at the interfaces of undoped and donor-doped NaNbO₃ with RuO₂ and ITO have been determined by means of photoelectron spectroscopy as a function of film thickness with in-situ sample preparation. The Fermi energies at the interfaces with RuO₂ are ~ 0.8 eV lower than those at the ITO interfaces. The difference is smaller than those observed for BaTiO₃, SrTiO₃, and Pb(Zr,Ti)O₃, which indicates the presence of a Fermi level pinning either at the NaNbO₃/RuO₂, at the NaNbO₃/ITO interface, or at both. Assuming unpinned Fermi levels at the ITO interfaces, the valence band maximum of NaNbO₃ would be at a similar energy than that of BaTiO₃ and SrTiO₃, while the valence band of NaNbO₃ would be lower if the Fermi level is unpinned at the interface with RuO₂. In both cases, a high electrical conductivity of donor-doped NaNbO₃ has to be expected if the energy gap of NaNbO₃ is of the magnitude determined by electron energy loss spectroscopy in this work and optical spectroscopy in literature (3.4 eV to 3.5 eV). In contrast, Ca- and Sr-doped NaNbO₃ are electrically insulating with a room temperature conductivity $< 10^{-10}$ S/cm. Field-dependent conductivity measurements with electric fields corresponding to a voltage drop of > 6 V per grain boundary do not evidence a varistor effect. It is therefore excluded that the high resistivity of donor-doped NaNbO₃ is caused by insulating grain boundaries. This is corroborated by impedance spectroscopy, which revealed no grain boundary contributions. It is therefore suggested that the conduction band minimum of NaNbO₃ is not 3.4 eV to 3.5 eV above the valence band maximum but substantially higher in energy and that optical measurements are strongly affected by a high exciton binding energy as it has also been discussed in literature for LiNbO₃.

ACKNOWLEDGMENTS

The presented work has been supported by the state of Hesse, Germany, within the LOEWE priority project FLAME (Fermi Level Engineering of Antiferroelectric Materials for Energy Storage and High Voltage Insulation Systems), by the German Academic Exchange Service (DAAD) through the PPP Slovenia, Project ID 57450108, by the Slovenian Research Agency (core funding P2-0105 and bilateral Project No. BI-DE/19-20-008), and by the European Union's Horizon 2020 research and innovation program under Grant Agreement No. 823717-ESTEEM3. We acknowledge U. Salzberger for TEM sample preparation, K. Hahn for support during EELS measurements, and W. Siegle for helpful suggestions. The DyScO₃ substrates have been grown in the working group Oxides and Fluorites at IKZ.

- [1] T. R. ShROUT and S. J. Zhang, Lead-free piezoelectric ceramics: Alternatives for PZT? *J. Electroceram.* **19**, 185 (2007).
- [2] J. Rödel, W. Jo, K. T. P. Seifert, E. M. Anton, T. Granzow, and D. Damjanovic, Perspective on the development of lead-free piezoceramics, *J. Am. Ceram. Soc.* **92**, 1153 (2009).
- [3] J. F. Li, K. Wang, F. Y. Zhu, L. Q. Cheng, and F. Z. Yao, (K,Na)NbO₃-based lead-free piezoceramics: Fundamental aspects, processing technologies, and remaining challenges, *J. Am. Ceram. Soc.* **96**, 3677 (2013).
- [4] W. Sakamoto, Y. Hamazaki, H. Maiwa, M. Moriya, and T. Yogo, Lead-free piezoelectric thin films of Mn-doped NaNbO₃-BaTiO₃ fabricated by chemical solution deposition, *Thin Solid Films* **518**, 4256 (2010).
- [5] B. C. Luo, H. Dong, D. Y. Wang, and K. X. Jin, Large recoverable energy density with excellent thermal stability in Mn-modified NaNbO₃-CaZrO₃ lead-free thin films, *J. Am. Ceram. Soc.* **101**, 3460 (2018).
- [6] R. N. Schwartz and B. A. Wechsler, Electron-paramagnetic-resonance study of transition-metal-doped BaTiO₃: Effect of material processing on Fermi-level position, *Phys. Rev. B* **48**, 7057 (1993).
- [7] R. A. Maier and C. A. Randall, Low temperature ionic conductivity of an acceptor-doped perovskite: II. Impedance of single-crystal BaTiO₃, *J. Am. Ceram. Soc.* **99**, 3360 (2016).
- [8] P. C. Bowes, J. N. Baker, and D. L. Irving, Site preference of Y and Mn in nonstoichiometric BaTiO₃ from first principles, *Phys. Rev. Materials* **4**, 084601 (2020).
- [9] H. Kishi, Y. Mizuno, and H. Chazono, Base-metal electrode-multilayer ceramic capacitors: Past, present and future perspectives, *Jpn. J. Appl. Phys.* **42**, 1 (2003).
- [10] N. H. Chan, R. K. Sharma, and D. M. Smyth, Nonstoichiometry in undoped BaTiO₃, *J. Am. Ceram. Soc.* **64**, 556 (1981).
- [11] H.-I. Yoo, C.-R. Song, and D.-K. Lee, BaTiO_{3-x}: Defect structure, electrical conductivity, chemical diffusivity, thermoelectric power, and oxygen nonstoichiometry, *J. Electroceram.* **8**, 5 (2002).
- [12] P. Erhart and K. Albe, Modeling the electrical conductivity in BaTiO₃ on the basis of first-principles calculations, *J. Appl. Phys.* **104**, 044315 (2008).
- [13] J. N. Baker, P. C. Bowes, J. S. Harris, and D. L. Irving, Mechanisms governing metal vacancy formation in BaTiO₃ and SrTiO₃, *J. Appl. Phys.* **124**, 114101 (2018).
- [14] N.-H. Chan and D. M. Smyth, Defect chemistry of donor-doped BaTiO₃, *J. Am. Ceram. Soc.* **67**, 285 (1984).
- [15] S. B. Zhang, S.-H. Wei, and A. Zunger, Microscopic Origin of the Phenomenological Equilibrium “Doping Limit Rule” in *n*-Type III-V Semiconductors, *Phys. Rev. Lett.* **84**, 1232 (2000).
- [16] W. Walukiewicz, Intrinsic limitations to the doping of wide-gap semiconductors, *Phys. B: Condens. Matter* **302-303**, 123 (2001).
- [17] J. Robertson and S. J. Clark, Limits to doping in oxides, *Phys. Rev. B* **83**, 075205 (2011).
- [18] C. G. V. de Walle and J. Neugebauer, Universal alignment of hydrogen levels in semiconductors, insulators and solutions, *Nature (London)* **423**, 626 (2003).
- [19] J. M. Langer and H. Heinrich, Deep-Level Impurities: A Possible Guide to Prediction of Band-Edge Discontinuities in Semiconductor Heterojunctions, *Phys. Rev. Lett.* **55**, 1414 (1985).
- [20] A. Zunger, Theory of 3d transition atom impurities in semiconductors, *Annu. Rev. Mater. Sci.* **15**, 411 (1985).
- [21] A. Zunger, Practical doping principles, *Appl. Phys. Lett.* **83**, 57 (2003).
- [22] C. Linderålv, A. Lindman, and P. Erhart, A unifying perspective on oxygen vacancies in wide band gap oxides, *J. Phys. Chem. Lett.* **9**, 222 (2018).
- [23] A. Klein, Interface Properties of dielectric oxides, *J. Am. Ceram. Soc.* **99**, 369 (2016).
- [24] S. Balaz, Z. Zeng, and L. J. Brillson, Heterojunction band offsets and dipole formation at BaTiO₃/SrTiO₃ interfaces, *J. Appl. Phys.* **114**, 183701 (2013).
- [25] R. Moos, W. Menesklou, and K. H. Härdtl, Hall mobility of undoped *n*-type conducting strontium titanate single crystals between 19 K and 1373 K, *Appl. Phys. A* **61**, 389 (1995).
- [26] H. P. R. Frederikse and W. R. Hosler, Hall Mobility in SrTiO₃, *Phys. Rev.* **161**, 822 (1967).
- [27] R. Schafrank, S. Li, F. Chen, W. Wu, and A. Klein, PbTiO₃/SrTiO₃ interface: Energy band alignment and its relation to the limits of Fermi level variation, *Phys. Rev. B* **84**, 045317 (2011).
- [28] S. Li, J. Morasch, A. Klein, C. Chirila, L. Pintilie, L. Jia, K. Ellmer, M. Naderer, K. Reichmann, M. Gröting, and K. Albe, Influence of orbital contributions to valence band alignment of Bi₂O₃, Fe₂O₃, BiFeO₃, and Bi_{0.5}Na_{0.5}TiO₃, *Phys. Rev. B* **88**, 045428 (2013).
- [29] R. D. King-Smith and D. Vanderbilt, First-principles investigation of ferroelectricity in perovskite compounds, *Phys. Rev. B* **49**, 5828 (1994).
- [30] M. Cardona, Optical Properties and Band Structure of SrTiO₃ and BaTiO₃, *Phys. Rev.* **140**, A651 (1965).
- [31] G. Gouget, M. Duttine, E. Durand, A. Villesuzanne, V. Rodriguez, F. Adamietz, T. Le Mercier, M. D. Braidia, and A. Demourgues, Isolating the two room-temperature polymorphs of NaNbO₃: Structural features, optical band gap, and reactivity, *ACS Appl. Electron. Mater.* **1**, 513 (2019).
- [32] H. Kato, H. Kobayashi, and A. Kudo, Role of Ag⁺ in the band structures and photocatalytic properties of AgMO₃ (M: Ta and Nb) with the perovskite structure, *J. Phys. Chem. B* **106**, 12441 (2002).
- [33] G. Li, N. Yang, W. Wang, and W. F. Zhang, Band structure and photoelectrochemical behavior of AgNbO₃-NaNbO₃ solid solution photoelectrodes, *Electrochim. Acta* **55**, 7235 (2010).
- [34] G. H. Khorrami, A. Kompany, and A. Khorsand Zak, Structural and optical properties of (K,Na)NbO₃ nanoparticles synthesized by a modified sol-gel method using starch media, *Adv. Powder Technol.* **26**, 113 (2015).
- [35] J. Lv, T. Kako, Z. Li, Z. Zou, and J. Ye, Synthesis and photocatalytic activities of NaNbO₃ rods modified by In₂O₃ nanoparticles, *J. Phys. Chem. C* **114**, 6157 (2010).
- [36] H. Zhu, Z. Zheng, X. Gao, Y. Huang, Z. Yan, J. Zou, H. Yin, Q. Zou, S. H. Kable, J. Zhao *et al.*, Structural evolution in a hydrothermal reaction between Nb₂O₅ and NaOH solution: From Nb₂O₅ grains to microporous Na₂Nb₂O₆ · $\frac{2}{3}$ H₂O fibers and NaNbO₃ cubes, *J. Am. Chem. Soc.* **128**, 2373 (2006).
- [37] W. Chen, Y. Hu, and M. Ba, Surface interaction between cubic phase NaNbO₃ nanoflowers and Ru nanoparticles for enhancing visible-light driven photosensitized photocatalysis, *Appl. Surf. Sci.* **435**, 483 (2018).

- [38] P. Li, H. Abe, and J. Ye, Band-gap engineering of NaNbO_3 for photocatalytic H_2 evolution with visible light, *Int. J. Photoenergy* **2014**, 380421 (2014).
- [39] M. Pisarski, Hydrostatic pressure in kinetic phenomena in NaNbO_3 single crystals, *Phys. Status Solidi B* **101**, 635 (1980).
- [40] A. Molak, The influence of reduction in valency of Nb ions on the antiferroelectric phase transition in NaNbO_3 , *Solid State Commun.* **62**, 413 (1987).
- [41] W. Bak, C. Kus, and W. S. Ptak, The transport properties of polycrystalline NaNbO_3 determined from impedance spectra at very low frequencies, *Ferroelectrics* **115**, 105 (1991).
- [42] S. Lanfredi, A. C. M. Rodrigues, and L. Dessemond, Effect of porosity on the electrical properties of polycrystalline sodium niobate: I, Electrical conductivity, *J. Am. Ceram. Soc.* **86**, 2103 (2003).
- [43] A. Klein, C. Körber, A. Wachau, F. Säuberlich, Y. Gassenbauer, R. Schafrank, S. P. Harvey, and T. O. Mason, Surface potentials of magnetron sputtered transparent conducting oxides, *Thin Solid Films* **518**, 1197 (2009).
- [44] Y. Hermans, A. Klein, K. Ellmer, R. Van De Krol, T. Toupance, and W. Jaegermann, Energy-band alignment of BiVO_4 from photoelectron spectroscopy of solid-state interfaces, *J. Phys. Chem. C* **122**, 20861 (2018).
- [45] F. Chen, R. Schafrank, S. Li, W. Wu, and A. Klein, Energy band alignment between $\text{Pb}(\text{Zr,Ti})\text{O}_3$ and high and low work function conducting oxides - from hole to electron injection, *J. Phys. D: Appl. Phys.* **43**, 295301 (2010).
- [46] S. Li, F. Chen, R. Schafrank, T. J. M. Bayer, K. Rachut, A. Fuchs, S. Siol, M. Weidner, M. Hohmann, V. Pfeifer *et al.*, Intrinsic energy band alignment of functional oxides, *Phys. Status Solidi RRL* **8**, 571 (2014).
- [47] A. Amoureux, C. Fernandez, and S. Steuernagel, ZFiltering in MQMAS NMR, *J. Magn. Reson., Ser. A* **123**, 116 (1996).
- [48] See Supplemental Material at <http://link.aps.org/supplemental/10.1103/PhysRevMaterials.6.084404> for nuclear magnetic resonance spectroscopy and energy-dispersive x-ray spectroscopy results, polarization hysteresis loops measured at low frequencies, band gap energies measured by x-ray photoelectron spectroscopy, low frequency permittivity values, and x-ray photoelectron spectra of pure, Ca- and Sr-doped NaNbO_3 at an interface to ITO and RuO_2 .
- [49] Y. Gassenbauer, R. Schafrank, A. Klein, S. Zafeiratos, M. Hävecker, A. Knop-Gericke, and R. Schlögl, Surface states, surface potentials, and segregation at surfaces of tin-doped In_2O_3 , *Phys. Rev. B* **73**, 245312 (2006).
- [50] R. Giesecke, R. Hertwig, T. Bayer, C. A. Randall, and A. Klein, Modification of the cathodic Schottky barrier height at the RuO_2 cathode during resistance degradation of Fe-doped SrTiO_3 , *J. Am. Ceram. Soc.* **100**, 4590 (2017).
- [51] H. Wang, V. Srot, B. Fenk, G. Laskin, J. Mannhart, and P. A. van Aken, An optimized TEM specimen preparation method of quantum nanostructures, *Micron* **140**, 102979 (2021).
- [52] T. Malis, S. C. Cheng, and R. F. Egerton, EELS log-ratio technique for specimen-thickness measurement in the TEM, *J. Electron Microsc. Tech.* **8**, 193 (1988).
- [53] J. Park, S. Heo, J.-G. Chung, H. Kim, H. Lee, K. Kim, and G.-S. Park, Bandgap measurement of thin dielectric films using monochromated STEM-EELS, *Ultramicroscopy* **109**, 1183 (2009).
- [54] A. C. Sakowski-Cowley, K. Łukaszewicz, and H. D. Megaw, The structure of sodium niobate at room temperature, and the problem of reliability in pseudosymmetric structures, *Acta Crystallogr. B* **25**, 851 (1969).
- [55] V. A. Shuvaeva, M. Y. Antipin, S. V. Lindeman, O. E. Fesenko, V. G. Smotrakov, and Y. T. Struchkov, Crystal structure of the electric-field-induced ferroelectric phase of NaNbO_3 , *Ferroelectrics* **141**, 307 (1993).
- [56] J. Koruza, J. Tellier, B. Malič, V. Bobnar, and M. Kosec, Phase transitions of sodium niobate powder and ceramics, prepared by solid state synthesis, *J. Appl. Phys.* **108**, 113509 (2010).
- [57] S. Ji, H. Liu, Y. Sang, W. Liu, G. Yu, and Y. Leng, Synthesis, structure, and piezoelectric properties of ferroelectric and antiferroelectric NaNbO_3 nanostructures, *CrystEngComm* **16**, 7598 (2014).
- [58] K. E. Johnston, C. C. Tang, J. E. Parker, K. S. Knight, P. Lightfoot, and S. E. Ashbrook, The polar phase of NaNbO_3 : A combined study by powder diffraction, solid-state NMR, and first-principles calculations, *J. Am. Chem. Soc.* **132**, 8732 (2010).
- [59] R. D. Shannon, Revised effective ionic radii and systematic studies of interatomic distances in halides and chalcogenides, *Acta Crystallogr. A* **32**, 751 (1976).
- [60] K. N. S. Schuldt, H. Ding, J. C. Jaud, J. Koruza, and A. Klein, Influence of defects on the Schottky barrier height at $\text{BaTiO}_3/\text{RuO}_2$ interfaces, *Phys. Status Solidi A* **218**, 2100143 (2021).
- [61] S. Tashiro and K. Ishii, Grain size and piezoelectric properties of (Ba, K, Na) NbO_3 lead-free ceramics, *J. Ceram. Soc. Jpn.* **114**, 386 (2006).
- [62] J. Xing, Y. Huang, B. Wu, H. Liu, Z. Tan, Q. Chen, W. Zhang, D. Xiao, and J. Zhu, Energy storage behavior in ErBiO_3 -doped (K,Na) NbO_3 lead-free piezoelectric ceramics, *ACS Appl. Electron. Mater.* **2**, 3717 (2020).
- [63] C.-J. Peng and H.-Y. Lu, Compensation effect in semiconducting barium titanate, *J. Am. Ceram. Soc.* **71**, C-44 (1988).
- [64] S. Jida, T. Suemasu, and T. Miki, Effect of microwave heating on $\text{BaTiO}_3\text{:Nb}$ ceramics with positive temperature coefficient of resistivity, *J. Appl. Phys.* **86**, 2089 (1999).
- [65] B. Huybrechts, K. Ishizaki, and M. Takata, The positive temperature coefficient of resistivity in barium titanate, *J. Mater. Sci.* **30**, 2463 (1995).
- [66] J. Lee and K. Hong, Revisit to the origin of grain growth anomaly in yttria-doped barium titanate, *J. Am. Ceram. Soc.* **84**, 1745 (2001).
- [67] J. Hreščak, G. Dražić, M. Deluca, I. Arçon, A. Kodre, M. Dapiaggi, T. Rojac, B. Malič, and A. Bencan, Donor doping of $\text{K}_{0.5}\text{Na}_{0.5}\text{NbO}_3$ ceramics with strontium and its implications to grain size, phase composition and crystal structure, *J. Eur. Ceram. Soc.* **37**, 3015 (2017).
- [68] H. Guo, H. Shimizu, Y. Mizuno, and C. A. Randall, Domain configuration changes under electric field-induced antiferroelectric-ferroelectric phase transitions in NaNbO_3 -based ceramics, *J. Appl. Phys.* **118**, 054102 (2015).
- [69] M. H. Zhang, L. Fulanović, S. Egert, H. Ding, P. B. Groszewicz, H. J. Kleebe, L. Molina-Luna, and J. Koruza, Electric-field-induced antiferroelectric to ferroelectric phase

- transition in polycrystalline NaNbO_3 , *Acta Mater.* **200**, 127 (2020).
- [70] M. Kosec, B. Malic, A. Bencan, and T. Rojac, KNN-based piezoelectric ceramics, in *Piezoelectric and Acoustic Materials for Transducer Applications*, edited by A. Safari and E. Koray Akdogan (Springer Science+Business Media, 2008), Chap. 5, pp. 81–102.
- [71] S. Hillmann, K. Rachut, T. J. M. Bayer, S. Li, and A. Klein, Application of atomic layer deposited Al_2O_3 as charge injection layer for high-permittivity dielectrics, *Semicond. Sci. Technol.* **30**, 024012 (2015).
- [72] S. Miyazaki, H. Nishimura, M. Fukuda, L. Ley, and J. Ristein, Structure and electronic states of ultrathin SiO_2 thermally grown on $\text{Si}(100)$ and $\text{Si}(111)$ surfaces, *Appl. Surf. Sci.* **113-114**, 585 (1997).
- [73] W. G. Schmidt, M. Albrecht, S. Wippermann, S. Blankenburg, E. Rauls, F. Fuchs, C. Rödl, J. Furthmüller, and A. Hermann, LiNbO_3 ground- and excited-state properties from first-principles calculations, *Phys. Rev. B* **77**, 035106 (2008).
- [74] C. Thierfelder, S. Sanna, A. Schindlmayr, and W. G. Schmidt, Do we know the band gap of lithium niobate? *Phys. Status Solidi C* **7**, 362 (2010).
- [75] M. Kruczek, E. Talik, and A. Kania, Electronic structure of AgNbO_3 and NaNbO_3 studied by x-ray photoelectron spectroscopy, *Solid State Commun.* **137**, 469 (2006).
- [76] A. Molak, M. Paweczyk, J. Kubacki, and K. Szot, Nano-scale chemical and structural segregation induced in surface layer of NaNbO_3 crystals with thermal treatment at oxidising conditions studied by XPS, AFM, XRD, and electric properties tests, *Phase Transitions* **82**, 662 (2009).
- [77] M. L. López, I. Álvarez-Serrano, A. Galdámez, E. Rodríguez-Aguado, E. Rodríguez-Castellón, and Y. Saad, New dielectric anomalies in the A-site highly deficient Na_xNbO_3 electroceramics, *Ceram. Int.* **46**, 16770 (2020).
- [78] K. Szot, F. U. Hillebrecht, D. D. Sarma, M. Campagna, and H. Arend, Surface defect segregation in the perovskite-type ferroelectric KNbO_3 , *Appl. Phys. Lett.* **48**, 490 (1986).
- [79] K. Szot, J. Keppels, W. Speier, K. Besocke, M. Teske, and W. Eberhardt, Surface chemistry and molecular reactions on KNbO_3 single crystal surfaces, *Surf. Sci.* **280**, 179 (1993).
- [80] L. T. Hudson, R. L. Kurtz, and S. W. Robey, Surface core-level shifts of barium observed in photoemission of vacuum-fractured $\text{BaTiO}_3(100)$, *Phys. Rev. B* **47**, 10832 (1993).
- [81] X. L. Li, B. Chen, H. Y. Jing, H. B. Lu, B. R. Zhao, Z. H. Mai, and Q. J. Jia, Experimental evidence of the “dead layer” at Pt/BaTiO_3 interface, *Appl. Phys. Lett.* **87**, 222905 (2005).
- [82] X. L. Li, H. B. Lu, M. Li, Z. Mai, H. Kim, and Q. J. Jia, Characteristics of the low electron density surface layer on BaTiO_3 thin films, *Appl. Phys. Lett.* **92**, 012902 (2008).
- [83] J. E. Rault, G. Agnus, T. Maroutian, V. Pillard, P. Lecoeur, G. Niu, B. Vilquin, M. G. Silly, A. Bendounan, F. Sirotti, and N. Barrett, Interface electronic structure in a metal/ferroelectric heterostructure under applied bias, *Phys. Rev. B* **87**, 155146 (2013).
- [84] D. G. Popescu, N. Barrett, C. Chirila, I. Pasuk, and M. A. Husanu, Influence of hole depletion and depolarizing field on the $\text{BaTiO}_3/\text{La}_{0.6}\text{Sr}_{0.4}\text{MnO}_3$ interface electronic structure revealed by photoelectron spectroscopy and first-principles calculations, *Phys. Rev. B* **92**, 235442 (2015).
- [85] T. A. Morgan, M. Zamani-Alavijeh, S. Erickson, G. Story, W. Schroeder, A. Kuchuk, M. Benamara, and G. J. Salamo, Self-assembled stoichiometric barium titanate thin films grown by molecular beam epitaxy, *J. Cryst. Growth* **493**, 15 (2018).
- [86] J. L. Wang, S. J. She, F. Gaillard, G. Niu, B. Vilquin, and N. Barrett, Strain dependence of dissociative adsorption of H_2O on epitaxially strained, out-of-plane polarized, $\text{BaTiO}_3(001)$ thin films, *Thin Solid Films* **717**, 138428 (2021).
- [87] I. Spasojevic, G. Sauthier, J. M. Caicedo, A. Verdaguier, and N. Domingo, Oxidation processes at the surface of BaTiO_3 thin films under environmental conditions, *Appl. Surf. Sci.* **565**, 150288 (2021).
- [88] V. Craciun and R. K. Singh, Characteristics of the surface layer of barium strontium titanate thin films deposited by laser ablation, *Appl. Phys. Lett.* **76**, 1932 (2000).
- [89] J. D. Baniecki, M. Ishii, T. Shioga, K. Kurihara, and S. Miyahara, Surface core-level shifts of strontium observed in photoemission of barium strontium titanate thin films, *Appl. Phys. Lett.* **89**, 162908 (2006).
- [90] S. Li, A. Wachau, R. Schafraneck, A. Klein, Y. Zheng, and R. Jakoby, Energy level alignment and electrical properties of $(\text{Ba,Sr})\text{TiO}_3/\text{Al}_2\text{O}_3$ interfaces for tunable capacitors, *J. Appl. Phys.* **108**, 014113 (2010).
- [91] F. Chen, R. Schafraneck, A. Wachau, S. Zhukov, J. Glaum, T. Granzow, H. von Seggern, and A. Klein, Barrier heights, polarization switching and electrical fatigue in $\text{Pb}(\text{Zr,Ti})\text{O}_3$ ceramics with different electrodes, *J. Appl. Phys.* **108**, 104106 (2010).
- [92] D. M. Long, A. Klein, and E. C. Dickey, Barrier formation at BaTiO_3 interfaces with Ni and NiO, *Appl. Surf. Sci.* **466**, 472 (2019).
- [93] S. Li, C. Ghinea, T. J. M. Bayer, M. Motzko, R. Schafraneck, and A. Klein, Electrical properties of $(\text{Ba,Sr})\text{TiO}_3$ thin films with Pt and ITO electrodes: Dielectric and rectifying behaviour, *J. Phys.: Condens. Matter* **23**, 334202 (2011).
- [94] G. H. Jonker, Some aspects of semiconducting barium titanate, *Solid-State Electron.* **7**, 895 (1964).
- [95] W. Heywang, Semiconducting barium titanate, *J. Mater. Sci.* **6**, 1214 (1971).
- [96] D. M. Smyth, The defect chemistry of donor-doped BaTiO_3 : A rebuttal, *J. Electroceram.* **9**, 179 (2002).
- [97] S. Lany, J. Osorio-Guillén, and A. Zunger, Origins of the doping asymmetry in oxides: Hole doping in NiO versus electron doping in ZnO, *Phys. Rev. B* **75**, 241203(R) (2007).
- [98] H. Wardenga, K. N. S. Schuldt, S. Waldow, R. A. De Souza, and A. Klein, Surface potentials of acceptor- and donor-doped CeO_2 thin films and their relation to oxygen surface exchange, *Phys. Chem. Chem. Phys.* **24**, 1072 (2022).
- [99] Y. Hermans, S. Murcia-López, A. Klein, R. Van De Krol, T. Andreu, J. R. Morante, T. Toupance, and W. Jaegermann, Analysis of the interfacial characteristics of BiVO_4 /metal oxide heterostructures and its implication on their junction properties, *Phys. Chem. Chem. Phys.* **21**, 5086 (2019).
- [100] J. Daniels, K. H. Härdtl, and R. Wernicke, The PTC effect of barium titanate, *Philips Tech. Rev.* **38**, 73 (1979).
- [101] W. Heywang, Bariumtitanat als Sperrschichtableiter, *Solid-State Electron.* **3**, 51 (1961).
- [102] K. Eda, Zinc oxide varistors, *IEEE Electr. Insul. Mag.* **5**, 28 (1989).

- [103] G. Blatter and F. Greuter, Electrical breakdown at semiconductor grain boundaries, *Phys. Rev. B* **34**, 8555 (1986).
- [104] G. T. Mallick and P. R. Emtage, Current-voltage characteristics of semiconducting barium titanate ceramic, *J. Appl. Phys.* **39**, 3088 (1968).
- [105] S. H. Kim, H. W. Seon, H. T. Kim, J. G. Park, Y. Kim, and J. D. Byun, Effect of MnO addition on the electrical properties of Nb-doped SrTiO₃ varistor, *Mater. Sci. Eng. B* **60**, 12 (1999).
- [106] M. Kuwabara, H. Matsuda, and Y. Ohba, Varistor characteristics in PTCR-type (Ba,Sr)TiO₃ ceramics prepared by single-step firing in air, *J. Mater. Sci.* **34**, 2635 (1999).
- [107] T. Kolodiaznyi, A. Petric, and G. P. Johari, Models of the current-voltage dependence of BaTiO₃ with positive temperature coefficient of resistivity, *J. Appl. Phys.* **89**, 3939 (2001).
- [108] C. Fang, D. X. Zhou, and S. P. Gong, Voltage effect in PTCR ceramics: Calculation by the method of tilted energy band, *Phys. B: Condens. Matter* **405**, 852 (2010).
- [109] I. G. Hill, A. Kahn, Z. G. Soos, and R. A. P. Jr., Charge-separation energy in films of π -conjugated organic molecules, *Chem. Phys. Lett.* **327**, 181 (2000).
- [110] U. Weiler, T. Mayer, W. Jaegermann, C. Kelting, D. Schlettwein, S. Makarov, and D. Wöhrle, Electronic energy levels of organic dyes on silicon: A photoelectron spectroscopy study of ZnPc, F₁₆ZnPc, and ZnTPP on p-Si(111):H, *J. Phys. Chem. B* **108**, 19398 (2004).